Towards Sustainable Sulfide-Based All-Solid-State-Batteries: An Experimental Investigation of the Challenges and Opportunities Using Solid Electrolyte Free Silicon Anodes

Tobias Neumann,*[a] Lukas Alexander Dold,*[a] Alain Thomas Cerny,[a] Eric Tröster,[a] Michael Günthel,[a] Anna Fischer,[b, c] Kai Peter Birke,[d] Ingo Krossing,[b, c] and Daniel Biro[a, c]

Silicon is one of the most promising anode active materials for future high–energy lithium-ion-batteries (LIB). Due to limitations related to volume changes during de–/lithiation, implementation of this material in commonly used liquid electrolyte-based LIB needs to be accompanied by material enhancement strategies such as particle structure engineering. In this work, we showcase the possibility to utilize pure silicon as anode active material in a sulfide electrolyte-based all-solid-state battery (ASSB) using a thin separator layer and $LiNi_{0.6}Mn_{0.2}Co_{0.2}O_2$ cathode. We investigate the integration of both solid electrolyte blended anodes and solid electrolyte free anodes and explore the usage of non-toxic and economically viable solvents suitable for standard atmospheric conditions for the latter. To give an insight into the microstructural changes as well as the lithiation path inside the anode soft X-ray emission and X-ray photoelectron spectroscopy were performed after the initial lithiation. Using standard electrochemical analysis methods like galvanostatic cycling and impedance spectroscopy, we demonstrate that both anode types exhibit commendable performance as structural distinctions between two-dimensional and three-dimensional interfaces became evident only at high charge rates (8 C).

Introduction

Silicon has attracted growing attention as the most promising candidate for the next-generation anode active material for lithium-ion batteries. Silicon is non-toxic, widely available, and has a high theoretical specific capacity of 3578 mAh g^{-1} ($Li_{15}Si_4$) as well as a low working potential of 0.1–0.4 V vs. Li/Li$^+$.[1–3] However, the strong volume expansion of 280% during lithiation leads to particle pulverization and continuous disruption and reformation of the Solid Electrolyte Interphase (SEI) on the surface of newly exposed areas in lithium-ion batteries with liquid electrolytes.[4–6] The irreversible consumption of lithium and electrolyte components leads to the formation of a thick SEI layer and an increase in cell polarization, resulting in rapid capacity loss.[7] Various strategies have been developed and applied to counteract the degradation mechanisms of silicon-based anodes, including particle structure engineering, addition of electrolyte additives, application of novel binders, or pre–lithiation.[8–12]

In particular, the interface between silicon and the liquid electrolyte and the wetting of the active surface generated by particle pulverization followed by SEI formation on these surfaces are considered to be amongst the biggest challenges in the commercialization of silicon-based anodes.[13] The application of silicon-based anodes in all-solid-state-batteries has emerged as another promising approach due to the different interfacial interaction between the solid electrolyte and silicon particles.[14] Hitherto, the majority of publications in this research area focused on lithium-metal anodes. However, the application of lithium-metal anodes still faces significant challenges such as lithium-dendrite formation, unstable SEI-formation as well as impurities on the lithium interface resulting in high impedances or cell malfunction.[15,16]

Lithium-ion solid-state electrolytes exist in a variety of material classes.[17,18] One such class are thiophosphates with its most famous representatives being ß-Li_3PS_4, $Li_{10}MP_2S_{12}$ (M=Ge, Sn) and Argyrodite-Li_6PS_5X (X=Cl$^-$, Br$^-$, I$^-$). Thiophosphates (sulfides) are known for their high ionic conductivity (up to 10^{-2} S cm^{-1}) at room temperature as well as their great ductile properties. The latter allow for the formation of a well–connected interpenetration network within the electrodes, in addition to the subsequent densification of this network through the utilization of cold press procedures at moderate pressures (100–400 MPa).[14]

[a] T. Neumann, L. Alexander Dold, A. Thomas Cerny, E. Tröster, M. Günthel, D. Biro
Department of Electrical Energy Storage, Department of Sustainable Synthesis Products, Fraunhofer Institute for Solar Energy Systems ISE, Heidenhofstraße 2, 79110 Freiburg Germany
E-mail: tobias.neumann@ise.fraunhofer.de
lukas.alexander.dold@ise.fraunhofer.de

[b] A. Fischer, I. Krossing
Institute for Inorganic and Analytical Chemistry (IAAC), University of Freiburg, Albertstraße 21, 79104 Freiburg Germany <

[c] A. Fischer, I. Krossing, D. Biro
Freiburger Materialforschungszentrum (FMF), University of Freiburg, Stefan-Meier-Straße 21, 79104 Freiburg Germany

[d] K. Peter Birke
Chair for Electrical Energy Storage Systems, Institute for Photovoltaics (ipv), University of Stuttgart, Pfaffenwaldring 47, 70569 Stuttgart Germany

Batteries & Supercaps

Research Article
doi.org/10.1002/batt.202400412

**Chemistry
Europe**

European Chemical
Societies Publishing

The structural design of silicon-based anodes significantly influences the pathways of electrons and lithium ions within the cell. Lithium ions migrate through the electrolyte until they reach the interface with the electrode, where they form a silicon lithium alloy and then diffuse through the silicon lattice. Compared to a liquid electrolyte cell, the solid electrolyte does not fully wet a porous silicon electrode.[19] One way to provide sufficient transport pathways for lithium ions is to blend the silicon with the solid electrolyte during electrode production.[19–21] The resulting pathways through the anode enable a three-dimensional interface between the silicon particles and the solid electrolyte. This generally leads to increased rate capability but reduced energy densities due to the inactive solid electrolyte in the anode. Higher energy densities can be achieved with solid electrolyte free anodes, similar to the electrodes in liquid electrolyte cells. In this case, a planar two-dimensional interface is formed between the silicon particles and the solid electrolyte. Lithium diffusion within the electrode occurs through the interfaces of the active material particles.[21,22] Hence, Zhan et al. reviewed a wide variety of silicon-based solid-state batteries with two- and three-dimensional anode active material solid electrolyte interfaces.[4]

Huo et al. compared the cycling stability of a two-dimensional interface (Si-Anode|Li$_6$PS$_5$Cl-Separator) with a blended (three-dimensional) set-up to identify the changes in SEI-formation as a significant cause for the increase in cell impedance and rapid capacity decay.[23] In solid electrolyte free anodes, they observed a reduced degradation behavior due to the lack of SEI formation inside the anode, while maintaining sufficient ionic and electronic conductivity. In combination with Li$_2$B$_4$O$_7$ coated NMC cathodes with an areal capacity of 4.31 mAh cm^{-2}, a Li$_6$PS$_5$Cl pellet separator and a n/p ratio of 1.3 a capacity retention of 58.1% was achieved after 100 cycles. The cell was cycled at an initial stack pressure of 50 MPa at room temperature. Similar observations of reduced loss of lithium inventory by using two-dimensional anode solid electrolyte interfaces were reported recently.[13,24]

Tan et al. used a 99.9 wt.% micro–sized silicon anode (0.1 wt.% PVDF), a 700 µm thick Li$_6$PS$_5$Cl pellet and a dry processed NMC811 cathode protected by a lithium borate coating that yielded 80% capacity retention after 500 cycles with an areal capacity of 2 mAh cm^{-2}, a n/p ratio of 1.1 and a stack pressure of 50 MPa at room temperature.[22] Additionally, they investigated the influence of conductive additives in an anode containing silicon as well as a solid electrolyte and observed severe electrolyte decomposition when using 20 wt.% carbon black as a conductive additive compared to additive-free anodes.
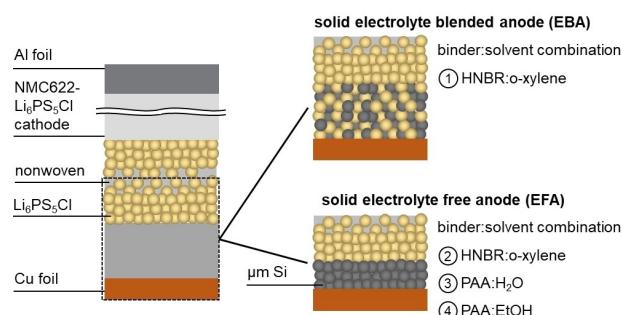
The removal of the solid electrolyte from the anode opens new ways of engineering silicon anodes for the implementation in ASSBs such as the use of non-toxic and environmentally friendly solvents in the slurry preparation, which additionally allows the anode slurry casting process to be performed under standard atmospheric conditions. Polyacrylic acid (PAA) is known to be a frequently used binder for silicon-dominant anodes in battery cells with carbonate-based electrolytes.[25,26] PAA can form strong adhesive bonds with silicon particles,

allowing it to accommodate the large volume changes of silicon during (de−)lithiation. In addition, PAA is soluble in water and can form hydrogen bonds, which give it a self-healing effect. Moreover, PAA is widely available at low costs.[25,27,28]

Herein, we present our most recent findings on the differences of solid electrolyte blended (EBA) and solid electrolyte free silicon anodes (EFA) for all-solid-state batteries. Utilizing pristine silicon with particles smaller than 5 µm (Figure S1), we focus on a straightforward producible material to assess the native performance of silicon inside an ASSB. To illustrate the structural differences between these two anodes, we recorded cross section SEM images in combination with energy-dispersive X-ray spectroscopy (EDX) mappings. The comparative evaluation of the effects of the two- and three-dimensional interfaces between the anode active material and the solid electrolyte was conducted through electrochemical testing including galvanostatic cycling, C-rate capability testing and impedance spectroscopy. A cell setup employing Li$_6$PS$_5$Cl infiltrated into a scaffold structure (nonwoven) as separator layer (~30 µm) and a casted layer of a LiNi$_{0.6}$Mn$_{0.2}$Co$_{0.2}$O$_2$:Li$_6$PS$_5$Cl blend as cathode was utilized for evaluating both anode types. While lithiation pathways of EBA are comparable with lithium-ion-batteries with liquid electrolytes, the lithiation of EFA is quite different due to the two-dimensional interface of the active material and the Li$_6$PS$_5$Cl. Therefore, we investigated the presence of lithium inside the cross section of a fully charged EFA using soft X-ray emission spectroscopy (SXES) and at the interface between Cu and EFA using X-ray photoelectron spectroscopy (XPS). Due to the surprisingly good performance of the EFA, we additionally investigated the use of non-toxic and environmentally friendly solvents in the slurry preparation while conducting the anode slurry casting process under standard atmospheric conditions. Electrodes processed with polyacrylic acid (PAA) dissolved in water and ethanol respectively were used for this evaluation. The possible oxidation of the silicon particle surface due to aqueous processing was evaluated using Raman and infrared (FTIR) spectroscopy.

Results and Discussion

Figure 1 shows a schematic representation of the anode slurry designs evaluated within the scope of this work. To enable a

Figure 1. Schematic overview of solid electrolyte blended, and solid electrolyte free anode designs evaluated within the scope of this work.

Batteries & Supercaps

Research Article
doi.org/10.1002/batt.202400412

Chemistry Europe
European Chemical
Societies Publishing

meaningful comparison, only the solvents, the binder, and the proportion of Li_6PS_5Cl particles in the anode were varied during this evaluation. Initially we evaluated a solid electrolyte blended anode (EBA) consisting of a blend of silicon and solid electrolyte as well as the binder, and a solid electrolyte free anode (EFA) consisting solely of silicon and the binder. Both anodes were processed in a slurry with a hydrogenated nitrile butadiene rubber (HNBR) binder and o-xylene as the solvent. The EBA is referred to as HNBR:o-xylene:LPSCl anode, while the EFA is referred to as HNBR:o-xylene. In the next step, we additionally investigated the use of PAA as a binder for EFAs, processed in water (PAA:H_2O) and ethanol (PAA:EtOH). The same separator (Li_6PS_5Cl infiltrated non-woven) and single crystal NMC622 cathode were used for all cells.

To evaluate the difference between a solid electrolyte blended and a solid electrolyte free anode, the EBA and EFA designs, both processed with HNBR as the binder, were compared. Figure 2 shows the cross section SEM images of the EBA and EFA in a cell stack. An overview of the entire cell stack can be found in Figure S2 (supporting information).
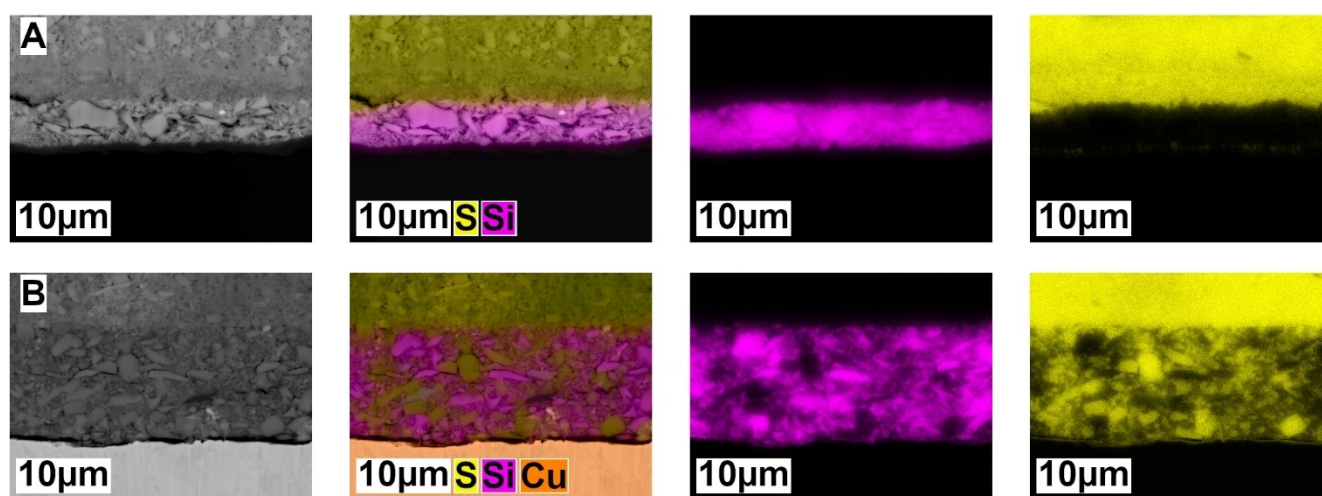
Both anodes were prepared aiming for the same areal loading (1 mg_{Si} cm^{-2}) in order to achieve equal capacities. The SEM images reveal that the EBA (11.44±0.29 μm) is approx. 3 times thicker than the EFA (3.85±0.32 μm). The values were calculated as the average of 15 measuring points. This is in good agreement with the theoretical value of a 2.5 times increase of thickness based on the mass ratios of 50 wt.% Si ($\rho = 2.32$ g cm^{-3}) and 50 wt.% Li_6PS_5Cl ($\rho = 1.64$ g cm^{-3}) selected for the solid electrolyte blended anode.[29] The individual element mappings in Figure 2B show a good distribution of silicon and Li_6PS_5Cl in the anode. It also confirms that blending both materials did not result in the facture of the micrometer–sized silicon crystallites (compare Figure S1).

The embedding of the silicon particles within Li_6PS_5Cl results in an interpenetrating solid electrolyte network which is expected to allow for a more uniform and homogeneous lithiation of the individual silicon particles during the charging of the battery cell. In contrast, the lithiation of the EFA occurs from the two-dimensional interface between the silicon of the anode and the Li_6PS_5Cl of the separator layer by lithium-ion diffusion through the silicon lattices as shown in Figure 2A. To investigate the influence of this structural difference on the electrochemical performance, galvanostatic measurements were conducted in battery cells with a thin separator layer (Li_6PS_5Cl infiltrated into a nonwoven) and a NMC622 cathode layer (single crystalline NMC particles blended with Li_6PS_5Cl).
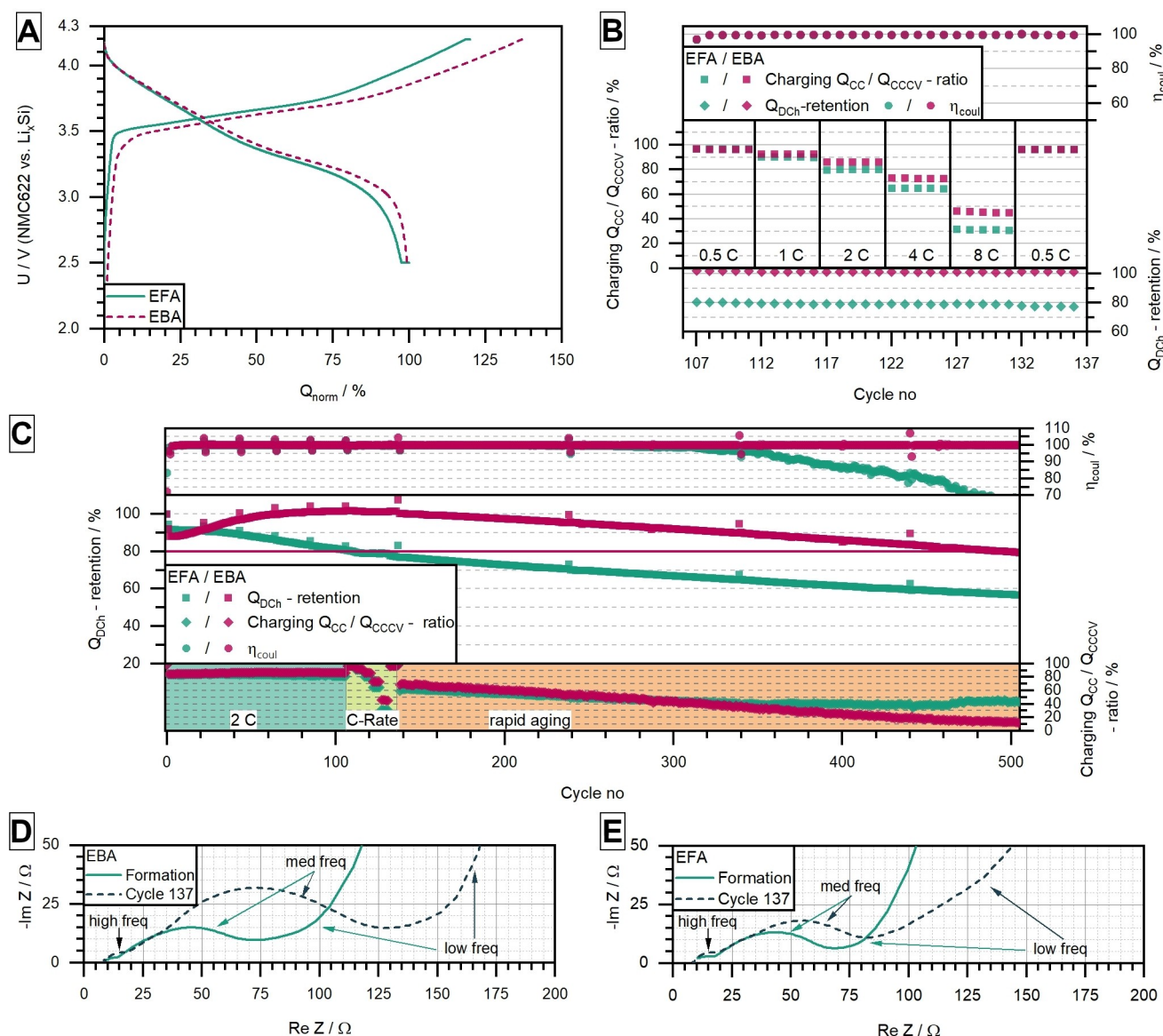
In accordance with the larger electrolytically contacted interface between silicon and Li_6PS_5Cl and a therefore intensified SEI formation, a lower initial coulombic efficiency of 72.1% is observed for the cell with the EBA, in contrast to 83.4% for the cell with the EFA (Figure 3A and C). Comparing the capacity retention of the formation cycle with the following cycle, a decrease to 92.2% for the cell with the EBA and to 94.5% for the cell with the EFA can be observed. This capacity drop is attributed to the increase in the C-rate to 2 C during charging. However, the cell containing the EBA is able to recover parts of the initial capacity in the subsequent cycles, resulting in a capacity retention of 104.5% in the energy test preceding the C-rate capability test in cycle 106. In contrast, for the cell with the EFA, a continuous capacity fade with a capacity retention of 83.2% can be observed after 106 cycles.

During the CC–CV charging cycles at a C-rate of 2 C (CV cut-off of 0.2 C), both the EBA and the EFA show a Q_{CC}/Q_{CCCV}-ratio of more than 80%. Clear differences in the proportions of the capacity achieved in the CC phase get visible in the C-rate capability test (Figure 3B). At 4 C, the EBA and the EFA achieve 73% and 65% of their capacity during the CC phase, respectively. At a charge rate of 8 C, this difference becomes even more pronounced. While the EBA is able to retain a Q_{CC}/Q_{CCCV}-ratio of 48% even at 8 C, the EFA drops to 34% at 8 C. We attribute this difference in C-rate capability to the structural differences between solid electrolyte blended and solid electrolyte free anodes.

Figure 2. Cross section SEM images in combination with EDX-mapping of overall elements as well as individual elemental mappings for S and Si for the HNBR: o–xylene EFA (A) and HNBR:o-xylene:LPSCl EBA (B).

Figure 3. Electrochemical evaluation of the HNBR:o-xylene:LPSCl EBA and the HNBR:o-xylene EFA in full cells. A) Potential curve (voltage vs. normalized capacity) of the formation normalized to the discharge capacity, B) C-rate capability test results ranging from C-rates of 0.5 C–8 C. C) Overview of the cycle life stability (separated in the regions of cycling at 2 C, C-rate capability testing and rapid aging), Q_{DCh} discharge capacity retention and Q_{CC}/Q_{CCCV}-ratio during charging. D) Nyquist-plots of the HNBR:o-xylene:LPSCl EBA and E) Nyquist-plots of the HNBR:o-xylene EFA in the charged state during formation as well as in cycle 137 (energy testing). All cells were tested at 50 °C.

The limitation of through–plane lithium-ion diffusion inside the partially lithiated silicon anode becomes significantly noticeable in our evaluation. Especially, at C-rates above 4 C the missing solid electrolyte network in the EFA is noticeable by an increased overpotential during dis–/charging.

While the C-rate capability test showed that both anode types should be capable of 4 C dis–/charging, a steady decline in the discharge capacity retention can be observed for both cells during the rapid aging test at 4 C (CV cut-off at 0.2 C). Interestingly, this decline is disrupted in each energy testing cycle, showcasing a limited delithiation of the anodes at high C-rates, which is in line with the phenomenon of lithium trapping reported in previous studies.[30] This effect is also evident from the jumps in the coulombic efficiency displayed in Figure 3C.
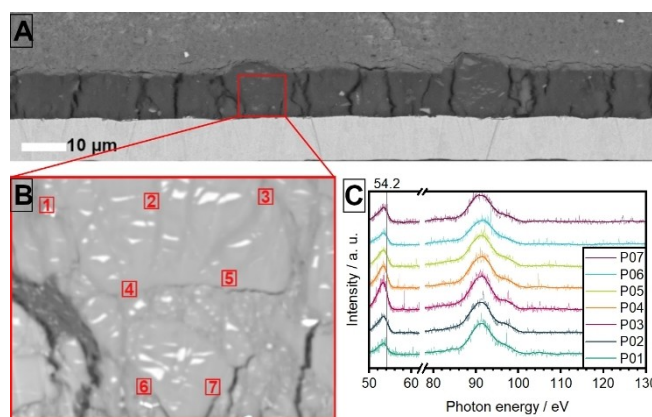
During the energy test cycles (CC–CV discharge at 0.2 C with a CV cut-off of 0.1 C), a coulombic efficiency > 100 % is achieved. In the subsequent cycle (at a once again increased C-rate), the trapping of Li in the anode active material is indicated by a coulombic efficiency < 98 %. Starting from a capacity retention of 83.2 % in the energy test after the C-rate capability test, the cell with the EFA falls below the capacity retention of 80 % during the subsequent rapid aging. At cycle 238 (energy test) the discharge capacity retention of the cell with the EFA only reaches 73.2 %, marking its already overdue end–of–life (EoL = 80 %). Even though EoL was reached, cycling was continued to investigate if critical failure occurs. From cycle 300 onwards a decline in coulombic efficiency is observed, indicating a over-charging and critical failure of the cell. In case of the EBA cell

Batteries & Supercaps

Research Article
doi.org/10.1002/batt.202400412

Chemistry
Europe

European Chemical
Societies Publishing

discharge capacity is up to 107.7% at cycle 137 (energy test after the C-rate capability test), demonstrating not only a high cycle stability but the curing of the initial loss of capacity as well. Nevertheless, rapid aging testing finally leads to a steady capacity loss of the EBA cell. Even though, at cycle 440 (energy test) capacity retention is still at 89.7% (showcasing a tremendous high cycling stability for silicon), a severe decline of Q_{CC} (Q_{CC}/Q_{CCCV}–ratio <20%) can be observed.

The main reason for the aging of the cells can be found in the Q_{CC}/Q_{CCCV}-ratio of the two anode types. In both cases this ratio declines as the capacity retention fades, suggesting an increase in internal impedance of the cells. To assess the increase in cell impedance, electrochemical impedance spectroscopy (EIS) was conducted in the charged state of the formation (cycle 0) and energy testing (before rapid aging, cycle 137). The impedance data (presented in Nyquist-plots) for cells with EBA (Figure 3D) and EFA (Figure 3E) can be divided into three regions: high, medium and low frequency. Due to individual differences a comparison between both cells is not possible. Instead, the difference in changes of the impedance between formation and cycle 137 can be compared, showing that these differ significantly. While the EFA cell only shows a slight increase of charge–transfer-impedance (pseudo-semi-circle) at medium frequencies, a severe increase is visible for the EBA cell in cycle 137. It is worth noting that in case of the EFA cell an additional change appeared in the low frequency region. These differences in impedance may be due to the different geometrical solid electrolyte | Si interfaces of the anodes, leading towards differences in SEI growth. While in case of the EFA cell SEI formation only took place at the interface of the separator and anode, it can be assumed that in the EBA cell this formation occurred at the surfaces of all silicon particles as shown by the distribution of the solid electrolyte in the anode in Figure 2. Since the volume of SEI is greater in case of EBA than in EFA (at least by a factor of 25, assuming a monodisperse particle size of 1 μm), an increase in total impedance in this region can be expected for the EBA, which is in line with the EIS-data. Due to the small interfacial area between the EFA and the solid electrolyte it can also be assumed that the impact of SEI formation is neglectable and the visible changes in cycle 137 are mainly affected by the growth of cathode–electrolyte interphase (NMC | Li_6PS_5Cl–Interphase).

To further evaluate the behavior of the EFA and the structural changes during lithiation, we evaluated the electrode cross section of a lithiated anode (formation cycle, cell charged to 4.2 V). To investigate the uniformity of lithiation of the EFA, we conducted SXES as well as XPS measurements.

Figure 4 shows an increase in thickness (anode) of 170% (from 3.85 ± 0.32 μm–10.34 ± 1.11 μm, averages of 15 measuring points) after the initial lithiation. According to Schmidt et al., this can be attributed to a $Li_{2.0-2.5}Si$ composition, which is in line with the targeted lithiation degree.[5] While Figure 2 showed a homogeneous distribution of silicon particles in the pristine anode, individual agglomerates and vertical cracks can be observed in the lithiated anode. This phenomenon has been reported previously by Yan et al. and is attributed to the volume change and amorphization of the silicon during lithiation.[31]
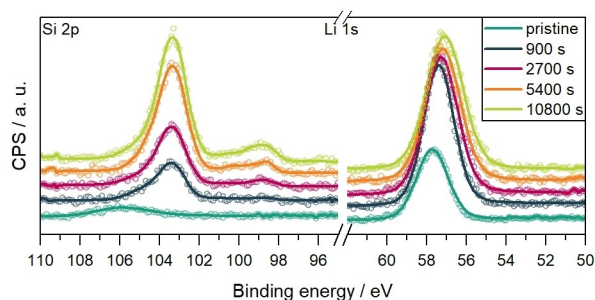

Figure 4. A) Cross section SEM image of the lithiated HNBR:o-xylene EFA, B) selected spots for SXES and C) measured spectra.

These structural changes can also cause delamination at the separator | EFA interface, which is the reason for the required stack pressure during cycling. SXES spectra were recorded at selected spots distributed over the lithiated EFA as shown in Figure 4B. Detected Li–Kα emission shifted below 54.2 eV (elemental lithium), verifying the presence of Li_xSi phases as previously reported by Lin et al.[32]

Since similar Li–Kα emission is detected at all measured spots, it can be concluded that a continuous lithiation through the electrode has occurred. In the $Si-L_{2,3}$-region a distinct signal can be measured at 92 eV with a low intensity shoulder at ~96 eV. Domi et al. reported a similar pattern while investigating the transition between "Li-poor" ($Li_{1-2}Si$) and "Li-rich" ($Li_{2-3.75}$) phases of lithiated Si particles via SXES.[33,34] These results comply with the degree of lithiation calculated from the volume expansion as well as the margin of error based on the capacity calculations, suggesting that a final lithiation of $Li_{x<2.5}Si$ was achieved during first lithiation. Also, since all patterns are similar in their entirety, it can be assumed that the Li_xSi distribution either follows a small gradient or is homogeneous in its entirety, which may be facilitated by the presence of fractions of small sized silicon particles (<1 μm) in the electrode.

Even though SXES already showed the continuous lithiation through the EFA, a distinct analysis of the degree of lithiation near the current collector could not be provided. Therefore, a charged cell (formation cycle) was disassembled and the copper foil was removed from the stack. The exposed surface was then examined using top-view XPS measurement (Figure 5). In addition, a pristine EFA cell was examined as well. Images of the as prepared samples are shown in Figure S3 (supporting information).

As shown in Figure 5 the freshly prepared surface of lithiated EFA shows a Si 2p signal of low intensity for silicon while the Li signal is distinct at 57.7 eV. The low intensity can be explained by impurities (possible originated during preparation of the sample) on the surface of the electrode. To remove this impurity a depth profile was conducted, resulting in an improve of Si 2p signal quality with each sputter step. Mean-

Batteries & Supercaps

Research Article
doi.org/10.1002/batt.202400412

Chemistry
Europe
European Chemical
Societies Publishing

Figure 5. Top view XPS data of the lithiated HNBR:o-xylene EFA specimen. Signal are shown for the Si 2p and Li 1s regions after different sputter times: pristine/0 sec (green), 900 sec (blue), 2700 sec (red), 5400 sec (orange) and 10800 sec (yellow).

while, the Li 1s signal slightly shifted towards a lower binding energy of 57.1 eV.

Linking this change to the decrease of O 1s signal at 533.8 eV and increase of 530.9 eV (Li_ySiO_x) signal (Figure S4, supporting information), it can be assumed that the degree of lithiation from outer to inner layers (mostly consisting of SiO_x in pristine specimen, Figure S5) is increasing.[35] At certain depth, lithiated Si, as indicated by the Si 2p signal at 98.4 eV (pure Si 2p signal at 99.4 eV, Figure S5, supporting information), can be found. These results clearly confirm that a continuous lithiation occurred through the EFA during charging.

It was already reported by Tan et al. and Huo et al. that solid electrolyte free silicon anodes, using untreated micrometer-sized silicon particles, achieve good cycling stability over several hundred cycles in ASSBs at high C-rates.[22,23]

However, to the best of our knowledge, this is the first time that solid electrolyte free anodes based on untreated silicon particles are evaluated in combination with a thin separator layer (~30 μm) and a NMC622 cathode. In Table 1 we show the impact of using either EFA or EBA on the energy density (cell level) and the required amount of Li_6PS_5Cl per kWh of energy. The areal capacity of 2 mAh cm^{-2} corresponds to the cell data shown in Figure 3, while the areal capacity of 4 mAh cm^{-2} is based on an assumed value for an industry-oriented cell design. The calculations reveal that by using EFAs the total amount of electrolyte needed can be reduced by 16% for anodes with an areal capacity of 2 mAh cm^{-2} and by 21% in case of 4 mAh cm^{-2}. This results in an energy density increase of 7% and 11%, respectively. In addition to the reduced requirements (e.g. dew

point) during anode production a significant reduction of costs can be expected.

Besides the economic advantages, the removal of the solid electrolyte from the anode also opens new ways of engineering silicon anodes for the implementation in ASSBs. One of these approaches is the use of non-toxic and environmentally friendly solvents in the slurry preparation, which additionally allows the anode slurry casting process to be performed under standard atmospheric conditions. PAA was chosen as a binder for the further evaluation of solid electrolyte free anodes due to its solubility in water and its ability to form strong adhesive bonds with silicon particles. Since it was expected that aqueous slurry processing may affect the silicon surface, due to irreversible side reaction during cycling, a non-aqueous slurry containing ethanol as solvent was also prepared.

Figure 6 shows the data from the electrochemical evaluation of the three solid electrolyte free anodes HNBR:o-xylene, PAA:H_2O, and PAA:EtOH. The cell data shown for the HNBR:o-xylene EFA are identical to the ones presented in Figure 3 and are displayed and referred to here again for reference.

Surprisingly, the three cells show a comparable initial coulombic efficiency of 83.4% for HNBR:o-xylene, 83.4% for PAA:H_2O, and 82.6% for the PAA:EtOH solid electrolyte free anode. Due to the oxidation of the silicon surface during aqueous slurry processing, a reduced initial coulombic efficiency for the cell with the PAA:EtOH EFA was expected. Raman and attenuated total reflectance infrared (ATR-IR) spectroscopy were conducted on the surface of the three pristine EFA electrodes. Figure S6 (supporting information) shows the spectra without any significant difference between the three electrodes. However, the comparison of the potential profiles of the three EFAs (Figure 6**A**) shows an overpotential for the cell with the PAA:H_2O EFA.
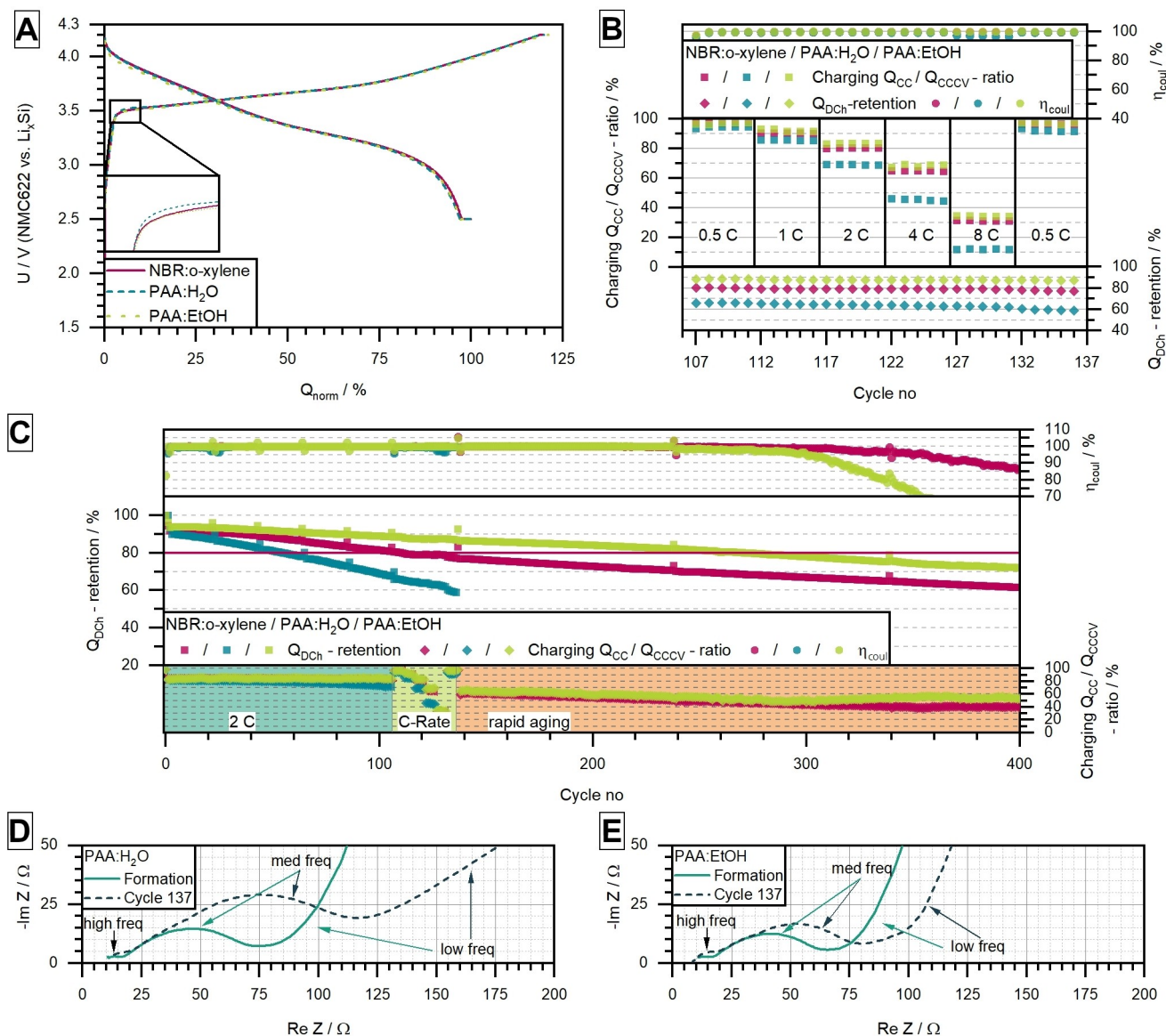
Comparing the discharge capacity retention of the formation cycle with the second cycle, a decrease to 93.3% and 96.5% can be observed for the PAA:H_2O and PAA:EtOH EFA, respectively. Similar to the HNBR:o-xylene EFA, the two anodes based on the PAA binder exhibit a continuous capacity fade. However, the extent of degradation between the three EFA types differs significantly. The cell with the aqueous processed PAA:H_2O anode shows the fastest capacity loss and has a capacity retention of 80.2% in the energy test in cycle 64 and 70.0% in the energy test (cycle 106) before the C-rate capability test, thus reaching its end of life criteria early. The C-rate capability test was nevertheless conducted for the cell, but it was not subjected to the subsequent rapid aging at 4 C. The

Table 1. Simulation of total electrolyte share inside an ASSB using an EBA and an EFA.			
Anode (simulated* based on meas. Data)	Electrolyte content/wt.–% (anode/separator/cathode)	Energy density/Wh·kg(cell)$^{-1}$	calculated electrolyte content per energy/kg·kWh^{-1}
EBA (2 mAh cm^{-2})	15.1/49.5/35.4	232	1.27
EBA (4 mAh cm^{-2})	20.2/32.7/47.1	287	0.95
EFA (2 mAh cm^{-2})	0/57.2/42.8	248	1.07
EFA (4 mAh cm^{-2})	0/42.0/58.0	318	0.75
*Possible overpotentials were excluded for the simulation. Full details on the simulation can be found in the supporting information.			

Figure 6. Electrochemical evaluation of the HNBR:o-xylene, PAA:H$_2$O and PAA:EtOH EFA in full cells. A) Potential curve (voltage vs. normalized capacity) of the formation normalized to the discharge capacity with an inset of the early charging region (0–10%), B) C-rate capability test results ranging from C-rates of 0.5 C–8 C. C) Overview of the cycle life stability (separated in the regions of cycling at 2 C C-rate capability testing and rapid aging), Q$_{DCh}$ discharge capacity retention and Q$_{CC}$/Q$_{CCCV}$ ratio during charging. D) Nyquist-Plots of the PAA:H$_2$O EFA and E) Nyquist-plots of the PAA:EtOH EFA in the charged state during formation as well as in cycle 137 (energy testing). All cells were tested at 50 °C.

cell with the PAA:EtOH EFA shows a capacity retention of 91.0% and a Q$_{CC}$/Q$_{CCCV}$-ratio of 85.1% in the energy test in cycle 106, outperforming the HNBR:o–xylene EFA (capacity retention of 83.2% and Q$_{CC}$/Q$_{CCCV}$-ratio of 82.6%).

Due to the two-dimensional interface between the active material and the electrolyte, the C-rate capability of the two PAA EFAs is comparable to that of the HNBR:o-xylene EFA. The PAA:H$_2$O and PAA:EtOH EFA show a Q$_{CC}$/Q$_{CCCV}$-ratio of 48% and 69% at 4 C, as well as 15% and 37% at 8 C, respectively. As previously concluded for the HNBR:o-xylene EFA, the C-rate during cycling should not exceed 4 C in order to achieve adequate performance of the cells with reasonable CC-phase proportions > 40%. The kinetically induced trapping of lithium

can be observed as previously described in the trends of coulombic efficiency and capacity retention for all three EFAs.

During rapid aging, both the HNBR:o-xylene and the PAA:EtOH EFA, starting from a capacity retention of 83.2% and 92.7% in the energy test in advance of rapid aging respectively, show an almost linear decline in capacity retention. However, the capacity fade of the PAA:EtOH EFA is less pronounced. In the energy test in cycle 339, the cell reached its end-of-life criteria revealing a discharge capacity retention of 79.2%.

EIS-measurements were conducted in the charged state during formation (cycle 0) and in the energy test before rapid aging (cycle 137). The Nyquist plots of the three EFA-type cells are shown in Figure 3E and Figure 6(D + E).The changes in impedance between formation and cycle 137 of the HNBR:o–

Batteries & Supercaps

Research Article
doi.org/10.1002/batt.202400412

Chemistry Europe
European Chemical
Societies Publishing

xylene and PAA:EtOH EFA are quite similar, with the exception of a slightly smaller increase in impedances for the PAA:EtOH EFA, which is expected due to the higher capacity retention. These results indicate that an analogical aging process occurred in both cases. However, the PAA:H_2O EFA (Figure 6D) shows a different pattern, as the changes in impedance are quite similar to the ones of the EBA, suggesting the formation of a Li-conductive interphase between the Si-particles. This is in line with the strong aging behavior of the cells since this interphase reduces the electrical contact between the Si-particle and disrupts the continuous lithiation of the anode.

In summary, based on the results from the electrochemical evaluation and the obtained cycling stability it can be said that the PAA:EtOH anode in particular seems to be a promising approach for a solid electrolyte free anode design in ASSBs. Due to the good performance of the PAA:EtOH EFA in the all-solid-state battery, the anode was also investigated in a cell with liquid electrolytes. Figure S7 (supporting information) reveals that the electrodes already fail in the formation cycle. While a charge capacity of 187.8 mAh g^{-1} can still be obtained, only 17.5 mAh g^{-1} can be achieved during delithiation (averaged values of three cells). Due to the lack of sufficient stack pressure in the liquid battery cell, the anode proves to be unsuitable for use in a LIB with liquid electrolytes. Poetke et al. observed similar results when comparing silicon-based active materials in battery cells with liquid and solid electrolytes, attributing this to the higher irreversible consumption of lithium due to SEI formation caused by the penetration of the active material through the liquid electrolyte.[36] This illustrates the different challenges that exist for LIBs with liquid electrolytes and ASSBs.

Conclusions

Our study reveals that both, solid electrolyte blended anodes as well as solid electrolyte free anodes can be effectively integrated into sulfide based ASSB full cells with a thin self-standing separator layer (<30 μm) and a single crystal NMC622 cathode. By employing cross section SEM in combination with SXES and XPS measurements, we were able to demonstrate a continuous lithiation of the entire solid electrolyte free anode (EFA). While both anodes performed well, the structural differences between the two and three-dimensional interfaces became particularly apparent at high C-rates. Nevertheless, good performance of the HNBR:o-xylene EFA, especially at C-rates <4 C was observed, prompting further investigation into environmentally friendly, non–toxic and economically favored solvents that can be used effectively under standard atmospheric conditions.

This enabled the utilization of PAA as a binder, which is considered promising due to its ability to form strong adhesive bonds with silicon particles, particularly for silicon dominant anodes. While an aqueous-based slurry with PAA binder (PAA:H_2O EFA) led to increased impedances and reduced stability during cycling, possibly due to the reaction of water with the silicon surface, the PAA:EtOH EFA resulted in further improvement in cycle stability compared to HNBR:o-xylene EFA. Overall, the

findings suggest electrolyte free silicon anodes offer a promising direction for reduction of production cost and risk, sustainability as well as cell cost of future sulfide-based all-solid-state-batteries.

Experimental Section

Electrode Fabrication and Cell Assembly

For the preparation of solid electrolyte free anodes, binder stock solutions (10 wt.%) of hydrogenated nitrile butadiene rubber (HNBR, Therban®LT1707, Acrylonitrile: 17 wt.%, Arlanxeo, dried at: <50 mbar, min. 12 h, 50 °C) in o-xylene (99%, extra dry, Thermo Fisher Scientific) and polyacrylic acid (M_w~450000, Sigma-Aldrich) in deionized water or ethanol (99.5%, extra dry, Thermo Fisher Scientific) were prepared. The anode slurry was obtained by wet milling micrometer-sized silicon (99.99%, 1 μm, Nanografi Nano Technology, dried at: <50 mbar, min. 12 h, 150 °C), the binder stock solution, and the respective solvent in a mixer mill (MM 500 control, Retsch) at 15 Hz for 1 hour. The mass ratios were chosen to obtain an electrode composition of 97 wt.% silicon and 3 wt.% binder. The wet milling of the HNBR:o-xylene slurry was carried out under argon atmosphere. The PAA:EtOH slurry was milled under argon atmosphere for safety reasons, but casted under atmospheric air. The PAA:H_2O slurry was fully processed under standard atmospheric conditions.

For the preparation of solid electrolyte blended anodes, 50 wt.% Li_6PS_5Cl (Argyrodite-structured, NEI Corporation) and 50 wt.% Si were dispersed in o-xylene and ball milled for four times at 15 Hz for 3 hours, interrupted by 10 min breaks. Subsequently the dispersion was dried under vacuum at 50 °C and sieved through a 300 μm mesh size sieve. Slurry processing of the as obtained composite was performed as described above. HNBR:o-xylene-based anodes were processed in an argon filled glovebox (E-Line, GS Glovebox System) at O_2 < 1 ppm and H_2O < 1 ppm.

Anode slurry casting was performed using a doctor blade (coating thickness 30–40 μm for solid electrolyte free and 95 μm for solid electrolyte blended anodes) and a film applicator on a copper foil (9 μm, MSE Supplies) to achieve an areal capacity of 1.8–2.6 mAh cm^{-2} assuming a specific capacity of 2000 mAh g^{-1} for the silicon. The positive effect of partial lithiation (below the theoretical capacity of silicon) on cycle stability has already been demonstrated in other studies.[37] After casting, the HNBR:o-xylene-based electrodes were dried at room temperature in the glovebox for one hour and subsequently for at least 30 minutes under vacuum. The PAA:H_2O and PAA:EtOH-based slurries were dried under atmospheric air for one hour at room temperature and then for >12 hours at 40 °C. Dried anodes were cut to a 5.8×4.5 cm^2 format to determine the average areal mass loading of 0.9–1.3 (EFA) and 2.2–2.7 (EBA) mg·cm^{-2}. It is to be noted that the copper foil has a declared areal density of 8.5–9.0 mg cm^{-2} and that due to the small–scale processes inaccuracies inside the electrodes are inevitable. Both effects impact the mass loading significantly, which is the reason for the wide margin of error.

The thin separator layer (~30 μm) was prepared by infiltration of PET nonwoven (Freudenberg Technology) via doctor blade casting from both sides with a dispersion consisting of 98 wt.% Li_6PS_5Cl and 2 wt.% HNBR (taken from stock solution) dispersed in o-xylene (ca. 0.95 g(LPSCl)/ml).

Cathodes consisting of 79.2 wt.% single crystal $Ni_{0.6}Mn_{0.2}Co_{0.2}O_2$ (NMC622, D_{50}=3–6 μm, MSE Supplies, dried at: <50 mbar, min. 12 h, 150 °C), 19.8 wt.% Li_6PS_5Cl, and 1 wt.% HNBR were prepared through a wet milling process similar to the one used for solid

Batteries & Supercaps

Research Article
doi.org/10.1002/batt.202400412

Chemistry
Europe

European Chemical
Societies Publishing

electrolyte blended anode slurries. To achieve an areal capacity of ~2.4 mAh cm^{-2} (assuming a specific capacity of 193 mAh g$_{NMC622}^{-1}$), cathode slurries were casted onto an aluminum foil (12 μm, MSE Supplies) using the doctor blade method (wet casting thickness: 240–250 μm). Dried cathodes were cut to a 5.8×4.5 cm^2 format to determine the average areal mass loading of 15.51 mg cm^{-2}. It is to be noted that as described above small–scale processes lead to a margin of error in the sheet, resulting in an error of ~10% between each cell. Due to the high amounts of errors cells will be compared using the formation discharge capacity (Q$_{F-DCh}$). Separators and cathodes were processed in an argon filled glovebox.

Cells were assembled in an ASC–A(+) cell casing (Sphere Energy) with either a polyetherimide (PEI) or a polyether ether ketone (PEEK) cell body and insulation sleeve (Sphere Energy). All steps were performed in an argon-filled glovebox. The cell assembly starts with punching the electrode coins with a diameter of 8 mm (anode and separator) or 7 mm (cathode) and the centered stacking in the insulation sleeve (stacking order: stainless steel plate (d = 8 mm, t = 0.5 mm), anode, separator, cathode), followed by pressing the stack with a force of 5 kN. Then, a PTFE O-ring (t = 100 μm, d$_o$ = 8 mm, d$_i$ = 7.2 mm) is placed around the cathode, a second metal plate is placed on top, and the stack is pressed with a force of 20 kN. Afterwards, three coins made of aluminum foil (d = 8 mm, t = 12–15 μm) are placed between the cathode and the upper metal plate for electrical conductivity and a homogeneous pressure distribution. Figure S8 (supporting information) shows a schematic overview of the assembled battery cell. The sleeve is then assembled into the cell casing and closed by tightening 6 screws (Quality: 12.9) slightly. After heating the cell to 50 °C for at least one hour, the upper screws are tightened using a torque of 5.8 Nm to ensure a tight fit. For each material two cells were assembled and characterized. In case of differences between the individual cells, the best performing one was chosen for overall comparison. All cells are shown in Figure S9–S12 (supporting information).

To additionally investigate the performance of the anodes in a lithium-ion battery with liquid electrolytes, 18 mm coins of the PAA: EtOH electrode were punched out. The electrodes were assembled in combination with a NMC622 cathode (2 mAh cm^{-2}, Customcells), a FS-5P separator (EL Cell), and 200 μl electrolyte (1 M LiPF$_6$ in EC:EMC:FEC: VC 26.4:61.6:10:2 by wt., E-Lyte Innovations) in a PAT-Cell (EL-Cell).

Electrochemical Characterization

Electrochemical measurements were performed on a Neware BTS4000 series battery tester at 50 °C in a potential window of 2.5 V–4.2 V. Formation of the cells was performed by CC–CV dis-/charging at a current of 38.6 mA g$_{NMC622}^{-1}$ and a cut-off of 19.3 mA g$_{NMC622}^{-1}$. The resulting discharge capacity (Q$_{DCh}$) was determined and used for defining the C-Rate (1 C = Q$_{DCh}$·h^{-1}). Following the initial charging, the cells were rested for at least 5 hours. Afterwards, recharged and hold at 4.2 V until a cut-off of 20 μA was reached, ensuring a pseudo thermodynamic equilibrium of the cells. At a bias of 4.2 V electrochemical impedance spectroscopy was performed in the range of 12 MHz–10 mHz (20 steps/dec (10 times/step) above 66 Hz, 2 steps/dec (2 times/step) below 66 Hz) using a Zahner Zennium X. Obtained data were refined to 6 MHz–10 mHz using the software Zahner Analysis 3.2.1. After the EIS measurement the cells were discharged at the C–rates given above.

The cycling of the cells was performed in five intervals of 20 cycles each, with a CC–CV charge and discharge at 2 C (CV cut-off of 0.2 C for dis-/charge). Before and after these intervals, an energy test was conducted with a CC–CV charge at 2 C (CV cut-off of 0.2 C) and a CC–CV discharge at 0.2 C (CV cut-off of 0.1 C). Following the five interval cycles a C-rate capability test was conducted with CC–CV

charge and discharge for five cycles each at 0.5 C, 1 C, 2 C, 4 C, 8 C, 0.5 C (CV cut-off of 0.2 C) and finished by a charging at 0.2 C (CV cut-off of 0.1 C) and including EIS measurement at 4.2 V (parameters were set identical to the measurement in the formation cycle). Selected cells were then discharged at 0.2 C (CV cut-off at 0.1 C) followed by a rapid aging test with a CC–CV dis-/charge at 4 C (CV cut-off of 0.2 C for dis-/charge). After every 100 cycles, an energy test was performed with a CC–CV charge at 4 C (CV cut-off of 0.2 C) and a CC–CV discharge at 0.2 C (CV cut-off of 0.1 C). The discharge capacities of the energy test were considered for the determination of the capacity retention of the cells.

Physicochemical Characterization Methods

Cross sections of the specimens were prepared by firstly cutting the pristine/charged ASSB (assembled as described above) with a scalpel inside the glovebox. Afterwards, the cells were adjusted to remove a 100 μm of the freshly cut cross section. All samples were transferred via an inert shuttle into a cryo-cross section polisher (CCP, JEOL IB-19520) and polished at room temperature, using an Ar ion beam with an accelerating voltage of 4 kV for 3.5 hours (gas flow 2.4–2.8) and a fine mode step of 30 minutes (gas flow 5) to prepare cross sections of the electrode stack.

SEM images were recorded using a JEOL JSM-IT800 Schottky Field Emission Scanning Electron Microscope with a back-scattered electron detector (BED) at a working distance of 10 mm and an acceleration voltage of 15 kV. Samples were transferred via an inert shuttle into the SEM.

EDX-Mapping was performed with an Oxford Ultim® Max 100 EDX (SDD size: 100 mm^2) detector using an acceleration voltage of 15 kV and a fixed working distance at 10 mm.

For SXES measurements, the working distance of the SEM was fixed at 10 mm. An accelerating voltage of 5 kV was applied. The beam current and the acquisition time were set to 5 nA and 100 s, respectively.

Photoelectron spectra were obtained using an EnviroESCA spectrometer from Specs GmbH (Phoibos 150 near-ambient pressure analyzer, 1D Delay Line Detector, monochromatic Al Kα radiation at 1486.6 eV, incident angle 55°). The prepared electrodes were transferred from the glove box and loaded under inert conditions into the XPS system. Survey spectra were measured utilizing a pass energy of 100 eV, 20 accumulations were measured to obtain high-resolution spectra at a pass energy of 50 eV. Charge compensation was required for XPS measurements of the compacted silicon sample, which was achieved by applying NAP conditions (water vapor at a pressure of 3 mbar). The resulting O 1s signal was used as binding energy reference (535.72 eV) for the compacted silicon sample; no binding energy referencing was required for the measurement of the electrode samples. A depth profile was generated using the ion gun GCIB 10S, Ionoptika (10 kV, Ar1000 cluster sputtering, 2 mm×2 mm, sputter interval 900 s).

The XPS data evaluation was done using CasaXPS. A Shirley background and Lorentzian line shapes were applied. A semi-quantitative analysis was done using relative sensitivity factors from CasaXPS.

A XploRa Plus Raman spectrophotometer with a confocal microscope (Horiba) was used to analyze the EFA with a 532 nm laser. The power was set to 1% mW and spectra from 0 cm^{-1}–1500 cm^{-1} with a 600 gr/mm grating were recorded with a measurement time of 50 seconds.

Attenuated total reflectance infrared (ATR-IR) spectroscopy was performed using a Bruker Alpha II Fourier-transform infrared spectrometer with a spectral resolution of 4 cm^{-1} and 24 repetitive

Batteries & Supercaps

Research Article
doi.org/10.1002/batt.202400412

Chemistry Europe
European Chemical
Societies Publishing

scans per background and sample measurement. Average values of triplicate measurements were used for the analysis. The acquired spectra were modified using a polynomial baseline correction in OPUS software (Bruker).

X-ray diffraction (XRD) measurements were conducted using a Rigaku Miniflex 600 with Cu Kα ration and a silicon monocrystal sample holder. The sample was covered by Kapton foil and the diffractogram was recorded between 10° and 80° 2θ using a step size of 0.02° with a measurement time of 1 s per step.

Supporting Information Summary

The authors have cited additional references within the Supporting Information.[38,39]

Conflict of Interests

The authors declare no conflict of interest.

Data Availability Statement

The data that support the findings of this study are available from the corresponding author upon reasonable request.

[1] C. Ban, K. Xu, *Lithium-Ion Batteries Enabled by Silicon Anodes*, Institution of Engineering & Technology, Stevenage **2021**, ISBN 978-1-78561-956-4, Eiditon 156, Chapter 1, pages 1–50.
[2] G. G. Eshetu, H. Zhang, X. Judez, H. Adenusi, M. Armand, S. Passerini, E. Figgemeier, *Nat. Commun.* **2021**, *12*, 5459.
[3] J. Li, J. R. Dahn, *J. Electrochem. Soc.* **2007**, *154*, A156.
[4] X. Zhan, M. Li, S. Li, X. Pang, F. Mao, H. Wang, Z. Sun, X. Han, B. Jiang, Y.-B. He, et al., *Energy Storage Mater.* **2023**, *61*, 102875.
[5] H. Schmidt, B. Jerliu, E. Hüger, J. Stahn, *Electrochem. Commun.* **2020**, *115*, 106738.
[6] X. H. Liu, L. Zhong, S. Huang, S. X. Mao, T. Zhu, J. Y. Huang, *ACS Nano* **2012**, *6*, 1522.
[7] G. G. Eshetu, E. Figgemeier, *ChemSusChem* **2019**, *12*, 2515.
[8] J. Sun, L. Huang, G. Xu, S. Dong, C. Wang, G. Cui, *Mater. Today* **2022**, *58*, 110.
[9] T.-W. Kwon, J. W. Choi, A. Coskun, *Chem. Soc. Rev.* **2018**, *47*, 2145.
[10] C. Wölke, B. A. Sadeghi, G. G. Eshetu, E. Figgemeier, M. Winter, I. Cekic-Laskovic, *Adv. Mater. Interfaces* **2022**, *9*, 2101898.
[11] J. Wu, Y. Cao, H. Zhao, J. Mao, Z. Guo, *Carbon Energy* **2019**, *1*, 57.
[12] M. Osiak, H. Geaney, E. Armstrong, C. O'Dwyer, *J. Mater. Chem. A* **2014**, *2*, 9433.
[13] S. Cangaz, F. Hippauf, F. S. Reuter, S. Doerfler, T. Abendroth, H. Althues, S. Kaskel, *Adv. Energy Mater.* **2020**, *10*, 2001320.
[14] Q. Zhang, D. Cao, Y. Ma, A. Natan, P. Aurora, H. Zhu, *Adv. Mater. (Deerfield Beach, Fla.)* **2019**, *31*, e1901131.
[15] D. Cao, X. Sun, Y. Li, A. Anderson, W. Lu, H. Zhu, *Adv. Mater. (Deerfield Beach, Fla.)* **2022**, *34*, e2200401.
[16] C. Hänsel, D. Kundu, *Adv. Mater. Interface* **2021**, *8*, 2100206.
[17] X. Bai, Y. Duan, W. Zhuang, R. Yang, J. Wang, *J. Mater. Chem. A* **2020**, *8*, 25663.
[18] W. Zhao, J. Yi, P. He, H. Zhou, *Electrochem. Energ. Rev.* **2019**, *2*, 574.
[19] M. Kim, H. Ahn, J. Choi, W. B. Kim, *Energy Tech.* **2023**, *11*, 2201321.
[20] J. Y. Kim, S. Jung, S. H. Kang, J. Park, M. J. Lee, D. Jin, D. O. Shin, Y.-G. Lee, Y. M. Lee, *Adv. Energy Mater.* **2022**, *12*, 2103108.
[21] J. Y. Kim, S. Jung, S. H. Kang, M. J. Lee, D. Jin, D. O. Shin, Y.-G. Lee, Y. M. Lee, *J. Power Sources* **2022**, *518*, 230736.
[22] D. H. S. Tan, H.-T. Chen, H. Yang, W. Bao, B. Sreenarayanan, J.-M. Doux, W. Li, B. Lu, S.-Y. Ham, B. Sayahpour, et al., *Science (N. Y., N. Y.)* **2021**, *373*, 1494.
[23] H. Huo, M. Jiang, Y. Bai, S. Ahmed, K. Volz, H. Hartmann, A. Henss, C. V. Singh, D. Raabe, J. Janek, *Nat. Mater.* **2024**, *23*, 543.
[24] J. Sakabe, N. Ohta, T. Ohnishi, K. Mitsuishi, K. Takada, *Commun. Chem.* **2018**, *1*, 24.
[25] A. Magasinski, B. Zdyrko, I. Kovalenko, B. Hertzberg, R. Burtovyy, C. F. Huebner, T. F. Fuller, I. Luzinov, G. Yushin, *ACS Appl. Mater. Interfaces* **2010**, *2*, 3004.
[26] L. Deng, Y. Zheng, X. Zheng, T. Or, Q. Ma, L. Qian, Y. Deng, A. Yu, J. Li, Z. Chen, *Adv. Energy Mater.* **2022**, *12*, 2200850.
[27] D. Jeong, J. Yook, D.-S. Kwon, J. Shim, J.-C. Lee, *Adv. Sci. (Weinheim, Baden-Wurttemberg, Ger.)* **2023**, *10*, e2302027.
[28] Y.-M. Zhao, F.-S. Yue, S.-C. Li, Y. Zhang, Z.-R. Tian, Q. Xu, S. Xin, Y.-G. Guo, *InfoMat* **2021**, *3*, 460.
[29] L. Zhou, K.-H. Park, X. Sun, F. Lalère, T. Adermann, P. Hartmann, L. F. Nazar, *ACS Energy Lett.* **2019**, *4*, 265.
[30] Y. Li, X. Zheng, Z. Cao, Y. Wang, Y. Wang, L. Lv, W. Huang, Y. Huang, H. Zheng, *Energy Storage Mater.* **2023**, *55*, 660.
[31] W. Yan, Z. Mu, Z. Wang, Y. Huang, D. Wu, P. Lu, J. Lu, J. Xu, Y. Wu, T. Ma, et al., *Nat. Energy* **2023**, *8*, 800.
[32] H. Lin, H. Noguchi, K. Uosaki, *Appl. Phys. Lett.* **2018**, *112*, 073903.
[33] Y. Domi, H. Usui, A. Ando, K. Nishikawa, H. Sakaguchi, *ACS Appl. Energy Mater.* **2020**, *3*, 8619.
[34] Y. Domi, H. Usui, N. Ieuji, K. Nishikawa, H. Sakaguchi, *ACS Appl. Mater. Interfaces* **2021**, *13*, 3816.
[35] J. Coyle, C. Apblett, M. Brumbach, J. Ohlhausen, C. Stoldt, *J. Vac. Sci. Technol.* **2017**, *35*, 061509.
[36] S. Poetke, F. Hippauf, A. Baasner, S. Dörfler, H. Althues, S. Kaskel, *Batteries Supercaps* **2021**, *4*, 1323.
[37] S. Poetke, S. Cangaz, F. Hippauf, S. Haufe, S. Dörfler, H. Althues, S. Kaskel, *Energy Tech.* **2023**, *11*, 2201330.
[38] D. N. Batchelder, R. O. Simmons, *J. Chem. Phys.* **1964**, *41*, 2324–2329.
[39] F. J. Günter, N. Wassiliadis, *J. Electrochem. Soc.* **2022**, *169*, 30515.